

A high-throughput Galectin-9 imaging assay for quantifying nanoparticle uptake, endosomal escape and functional RNA delivery

Michael Munson (✉ michael.munson@astrazeneca.com)

AstraZeneca <https://orcid.org/0000-0001-9927-8157>

Gwen O'Driscoll

AstraZeneca <https://orcid.org/0000-0002-1215-9989>

Andreia Silva

AstraZeneca

Elisa Lázaro-Ibáñez

AstraZeneca

Audrey Gallud

AstraZeneca

John Wilson

Vanderbilt University <https://orcid.org/0000-0002-9144-2634>

Anna Collén

Cardiovascular, Renal and Metabolism IMED Biotech Unit, AstraZeneca Gothenburg

Elin Esbjörner Winters

Department of Biology and Biological Engineering, Chalmers University of Technology

Alan Sabirsh

AstraZeneca (United Kingdom)

Article

Keywords: Endosomal Escape, Lipid Nanoparticle, mRNA, LGALS9, Galectin9, Drug Delivery, Beta-Sitosterol

Posted Date: November 20th, 2020

DOI: <https://doi.org/10.21203/rs.3.rs-94679/v1>

License:   This work is licensed under a Creative Commons Attribution 4.0 International License.

[Read Full License](#)

Version of Record: A version of this preprint was published at Communications Biology on February 16th, 2021. See the published version at <https://doi.org/10.1038/s42003-021-01728-8>.

1 **A high-throughput Galectin-9 imaging assay for quantifying nanoparticle**
2 **uptake, endosomal escape and functional RNA delivery.**

3 Michael J. Munson^{1*}, Gwen O'Driscoll¹, Andreia M. Silva², Elisa Lázaro-Ibáñez¹, Audrey Gallud³, John
4 T. Wilson⁴, Anna Collén⁵, Elin K. Esbjörner³, Alan Sabirsh^{1*}

5

6 ¹Advanced Drug Delivery, Pharmaceutical Sciences, BioPharmaceuticals R&D, AstraZeneca, Gothenburg, Sweden

7 ²Discovery Biology, Discovery Sciences, BioPharmaceuticals R&D, AstraZeneca, Gothenburg, Sweden

8 ³Division of Chemical and Biomolecular Engineering, Department of Biology and Biological Engineering, Chalmers University of Technology,
9 Gothenburg, Sweden

10 ⁴Department of Chemical and Biomolecular Engineering, Vanderbilt University, Nashville, Tennessee, USA

11 ⁵Projects, Research and Early Development, Cardiovascular, Renal and Metabolism, Biopharmaceuticals R&D, AstraZeneca, Gothenburg,
12 Sweden

13

14 **Keywords: Endosomal Escape, Lipid Nanoparticle, mRNA, LGALS9, Galectin9, Drug Delivery, Beta-**
15 **Sitosterol**

16

17

18 * Corresponding Authors:

19 Michael.Munson@astrazeneca.com

20 Alan.Sabirsh@astrazeneca.com

21

22 ABSTRACT

23 RNA-based therapies have great potential to treat many undruggable human diseases. However,
24 their efficacy, in particular for mRNA, remains hampered by poor cellular delivery and limited
25 endosomal escape. Advances in the development and rational optimisation of delivery vectors, such
26 as lipid nanoparticles (LNPs), are impeded by the limited availability of screening methods that probe
27 the intracellular processing of LNPs in sufficient detail.

28 We have developed a high-throughput imaging-based endosomal escape assay utilising a Galectin-9
29 reporter and fluorescently labelled mRNA to probe correlations between nanoparticle-mediated
30 uptake, endosomal escape frequency, and mRNA translation. This assay has, furthermore, been
31 integrated with a screening platform for nanoparticle formulation to optimise LNPs. We show that
32 Galectin-9 recruitment is a robust, quantitative reporter of endosomal escape events induced by
33 different mRNA delivery nanoparticles and small molecules. We also identify nanoparticles with
34 superior escape properties and demonstrate significant cell line variances in endosomal escape
35 response, highlighting the need for fine-tuning of delivery formulations for specific applications.

36 INTRODUCTION

37 Oligonucleotide therapies (including siRNA, antisense oligos (ASOs) and mRNA) are therapeutic
38 interventions that target or deliver protein-encoding mRNA; these can therefore modulate, with high
39 specificity, targets that are considered undruggable by classical small-molecule approaches or other
40 traditional modalities^{1,2}. Hydrophilic oligonucleotides cannot be readily taken up across cellular
41 membranes and are prone to degradation by endogenous nucleases, therefore the use of delivery
42 vectors for both protection and delivery is required³. Delivery systems such as lipid nanoparticles
43 (LNPs) or polymeric nanoparticles (PNPs) are being explored in an attempt to bolster the intracellular
44 delivery of oligonucleotides, however, these systems still have disadvantages concerning safety,
45 stability and most importantly delivery efficacy⁴. Despite progress in the development and design of
46 LNP and PNP vectors⁵, the delivery efficacy of short oligonucleotides using synthetic nanoparticles
47 remains poor. It has been estimated that only 1.5-3.5 % of siRNA cargo taken up by cells reach the
48 cytoplasm, with approximately half of the nucleotide cargo released when an endosomal disruption
49 event does occur^{6,7}. Oligonucleotides such as mRNA are significantly larger (~600-10,000 kDa) than
50 ASOs/siRNA (~4-14kDa), likely diminishing delivery yields even further⁵. Endosomal escape is
51 therefore one of the most significant bottlenecks for successful oligonucleotide delivery and
52 improving endosomal release is a key driver for delivery system design. Improving endosomal escape
53 will be of great importance for the development of oligonucleotide therapeutics, where there are
54 currently no commercial mRNA products available on the market today.

55 LNPs are of particular interest as delivery vectors due to their relative stability, low toxicity and ease
56 of large-scale preparation⁸. However, optimising the chemical and physical features of these entities
57 to improve functional delivery is a complex task. LNPs are typically comprised of four major lipid
58 components: an ionisable lipid, a sterol, a phospholipid and a lipidated polyethylene glycol (PEG). The
59 ionisable lipid has been the primary subject of development with a focus on combinatorial libraries
60 often used to identify new lipids^{9,10}. However, the undeniable importance of other components such

61 as the sterol or the PEG-lipid for increasing uptake, improving pharmacokinetics or modulating the
62 composition of the particles' coronas is being increasingly appreciated ¹¹⁻¹⁴. Optimising the relative
63 abundance of each of these components can also modulate potency by up to 7-fold ¹⁵, but to fully
64 explore all of these parameters requires fast and robust screening assays. Despite the central
65 importance of endosomal escape, there are currently limited established options to evaluate this
66 event in living cells ¹⁶.

67 Members of the Galectin (GAL/LGALS) family of proteins have been exploited as reporters of
68 endosomal escape in a variety of contexts. Galectins are primarily expressed in the cytosol and
69 contain carbohydrate recognition domains (CRDs) that bind to β -galactoside sugars ¹⁷. Galectins can
70 be recruited to endosomes in a CRD-dependent manner when membrane damage exposes β -
71 galactosides on the inner leaflet of the endosomal membrane to the cytosol ¹⁸. The exposure of β -
72 galactosides often occurs during host-pathogen interactions as a method of identifying damaged
73 cellular membranes and aims to assist in the clearance of pathogens ^{19,20}. GAL8/9 are also robustly
74 recruited to sites of endosomal damage in response to artificial delivery vehicles such as LNPs or
75 PNPs that induce endosomal escape as a mechanism of nucleotide cargo delivery ^{7,21}. Endosomal
76 escape induced localisation of GAL8 was shown to recruit autophagy adaptors as part of a clearance
77 response against *Salmonella* and therefore forms an important part of cellular host-defence ²⁰. GAL9
78 recruitment has no similarly reported perturbing effects on normal cellular function and was recently
79 reported to evoke a greater recruitment response to endolysosome damage than GAL3 or GAL8 ²².

80 To address the basic limitations of characterising nanoparticle function, we have developed a GAL9
81 based endosomal escape imaging assay to allow time-lapse live-cell recordings of endosomal damage
82 events. In combination with the use of fluorescently labelled nanoparticles, this single assay allows a
83 complete overview of nanoparticle trafficking from cellular uptake to endosomal escape and
84 ultimately mRNA translation to functional protein whilst also evaluating potential cellular toxicity
85 within a high-throughput format. We first demonstrate that this assay has a large signal window for

86 endosomal escape events, confirming its suitability as a screening assay. We subsequently validate
87 GAL9 recruitment in response to cell treatments with small molecules, LNPs and PNPs and highlight
88 cell line specific differences in sensitivity to endosomal escape. Finally, we demonstrate that this
89 assay can be combined with robotic LNP formulation, allowing for the first time, extensive and rapid
90 screening of nanoparticle formulations across multiple, biologically relevant parameters.

91 RESULTS

92 *Generation of mCherry-Galectin9 reporter cells*

93 We generated four stable mCherry-GAL9 reporter expression cell lines using the ObLiGaRe zinc-finger
94 nuclease (ZFN) knock-in strategy²³. Cell lines were transiently transfected with an *AAVS1*-targeting
95 ZFN plasmid and a donor construct encoding a puromycin resistance gene and mCherry-GAL9 under
96 the E1 α promoter (Fig. 1a). Positively integrated cells were selected with puromycin and flow-sorted
97 into pools with similar mCherry-GAL9 expression levels (Supplementary Fig. 1a,b). Gene copy number
98 analysis of HepG2 cells revealed on average ~2.3 integrated copies (Supplementary Fig. 2) of the
99 mCherry-GAL9 reporter compared to HeLa (2 copies), NCI-H358 (2.9 copies) and Huh7 (3.5 copies)
100 (Fig. 1b). The integration site was verified using primers to amplify between the *AAVS1* locus and the
101 reporter sequence, yielding the expected 251bp product (Fig. 1c). Cell expression of the mCherry-
102 GAL9 protein was verified by western blotting using an α -mCherry antibody for detection (Fig. 1d).
103 Two prominent bands were observed, corresponding to full-length (~70 kDa) and truncated (~50
104 kDa) mCherry-GAL9 (consistent with the loss of GAL9's C-terminal CRD (~20 kDa) due to protease
105 cleavage²⁴). Cells modified to express mCherry-GAL9 exhibited generally diffuse cytosolic mCherry
106 staining under standard growth conditions (Fig. 1e). Comparison of the cellular mCherry fluorescence
107 intensity by microscopy (Fig. 1f) supported the observations by western blot that HepG2 and NCI-
108 H358 cells expressed higher levels of protein than HeLa and Huh7 cells (Fig. 1d,f). This suggests that
109 cell-lineage related differences in reporter protein abundance exist that are not directly due to copy
110 number variation but may arise from differential regulation of galectin trafficking and secretion²⁵.
111 The protein abundance, however, was not decisive for assay function (see following).

112 *mCherry-GAL9 is recruited to small molecule induced damage*

113 To validate that mCherry-GAL9 can be recruited to sites of endolysosome damage, we exposed Huh7
114 mCherry-GAL9 cells to a series of small molecules known to induce endomembrane disruption
115 (Fig. 2a). We first used chloroquine, a cationic amphiphilic drug (CAD), which accumulates in late

116 endosomal compartments (Maxfield 1982) and that was recently used by Du Rietz et al. to study
117 endosome rupture in GFP-GAL9 expressing HeLa cells^{22,26}. Following administration of 0-80 μ M
118 chloroquine, we observed a clear, dose-dependent induction of large and bright mCherry-GAL9
119 positive structures with a maximum response after 8-12 h of treatment and at \sim 60-80 μ M, consistent
120 with the positive response obtained by Du Rietz et al (Fig. 2b,c). We then tested three additional
121 small molecules from a structurally-related family (UNC10217938A, UNC2383, and UNC4267 - Fig.
122 2a,b) which were previously identified to enhance the delivery of splice-switching oligonucleotides
123 and ASOs by inducing endomembrane permeabilisation^{27,28}. The response to UNC compounds was
124 rapid with maximal mCherry-GAL9 recruitment occurring at 1-3 h post-dosing (Fig. 2c); furthermore,
125 the effect was seen with a much lower dose (0-15 μ M) compared to chloroquine. UNC2383 was the
126 most potent compound with induction of large numbers of small mCherry-GAL9 structures already at
127 1.25 μ M (Fig. 2d). Our observations match both the timescale and the required doses to achieve
128 functional improvement of oligonucleotide delivery reported previously for UNC2383²⁹ and supports
129 that this effect is indeed functionally linked to endosome damage. Simultaneously, we inferred
130 cellular toxicity from the condensing of the nucleus that leads to smaller and more intense Hoechst
131 stained nuclear structures³⁰. All compounds tested elicited partial cellular toxicity that correlated
132 with the level of GAL9 recruitment (Fig. 2d). The ability to utilise nuclear morphology and intensity to
133 infer toxicity for simultaneous evaluation of compound safety is useful for future screening of
134 compound libraries to identify novel small molecules that can induce endosomal escape with
135 improved safety profiles.

136 Our data furthermore demonstrate that the mCherry-GAL9 recruitment assay can sensitively detect
137 differences in the endosomal damaging potencies of small molecule compounds and that their effect
138 does not require the presence of oligonucleotides.

139 We next determined the robustness of the mCherry-GAL9 recruitment assay in Huh7 cells by
140 calculating the Z' factor in response to UNC2383 treatment at 10 μ M. The Z' Factor is a measure of

141 separation between the minimum (undosed) and maximum response (UNC2383 10 μ M) often used in
142 the development of screening assays³¹. The Z' factor for Huh7 cells was calculated to +0.76; assays
143 rated above +0.5 are classified as excellent screening assays³¹. This validates that a large signal
144 window exists and that the mCherry-GAL9 reporter line enables robust detection of endosomal
145 damage.

146 *mCherry-GAL9 recruitment in response to mRNA delivery using LNPs*

147 The reporter cell lines were exposed to LNPs formulated by microfluidic mixing of Cy5-labelled,
148 EGFP-encoding mRNA and lipids, using the ionisable lipid DLin-MC3-DMA (MC3) to enable delivery⁹.
149 Uptake of MC3-LNPs was observed as a punctate Cy5 signal within both wild-type and mCherry-GAL9
150 cells, as demonstrated after 3 h of incubation with Huh7 cells (Fig. 3a). Quantification showed that
151 there was no difference in the number of intracellular Cy5-mRNA puncta between wild-type and the
152 mCherry-GAL9 cells (Fig. 3b), indicating that the introduction of the mCherry-GAL9 gene did not
153 affect cell uptake. Significant relocalisation of the initially diffuse cellular mCherry-GAL9 fluorescence
154 into bright punctate structures was observed following MC3-LNP uptake (Fig. 3a,b) and these often
155 co-occurred with the Cy5-mRNA signal (Fig. 3a). This indicates that the MC3-LNPs induce exposure of
156 β -galactoside ligands to the cytosol permitting mCherry-GAL9 binding. EGFP fluorescence, indicative
157 of successful cytosolic mRNA delivery, could also be observed from 3 h (Fig. 3a,b). There were also no
158 differences in EGFP intensity between wild-type and mCherry-GAL9 cells after 12 h (Fig. 3b).
159 Comparison of the levels of MC3-LNP uptake and EGFP expression in wild-type and mCherry-GAL9
160 Huh7 cells across time (up to 14 h after dosing) and across a dose-range (0.1-1 μ g/ml)
161 (Supplementary Fig. 3a,b) further emphasised that mCherry-GAL9 integration did not significantly
162 alter the normal cellular processing (uptake and mRNA delivery) of the LNPs. This indicates that
163 mCherry-GAL9 recruitment can be used to assess endosomal escape without significantly perturbing
164 the normal trafficking of LNPs.

165 We next tested whether the formation of mCherry-GAL9 puncta correlates with the levels of LNP
166 exposure and uptake, by testing a range of MC3-LNP doses across all reporter cell lines, and as a

167 function of incubation time, by high-content live-cell microscopy (Fig. 3c,d). Dose-dependent
168 increases in Cy5-mRNA structures, induction of mCherry-GAL9 structures and EGFP protein
169 produced, were observed as exemplified in Fig. 3c for HeLa mCherry-GAL9 cells after 10 hours of
170 exposure. The Cy5-mRNA and mCherry-GAL9 punctate structures were quantified over 0-14 h across
171 all reporter lines (Fig. 3d). Interestingly, the four cell lines displayed distinct differences in both the
172 degree and kinetics of MC3-LNP uptake, which was also reflected in the levels of endosomal escape.
173 Furthermore, the cells were different with respect to the level of EGFP produced across the dose
174 range tested, with liver lines Huh7 and HepG2 producing the highest levels of EGFP protein (Fig. 3d,
175 Supplementary Fig. 4a). HepG2 cells had a notably higher level of background autofluorescent
176 structures appearing in the mCherry and Cy5 channels, however, LNP-induced changes were still
177 observable above this background level (Fig. 3d).

178 Comparison of reporter lines demonstrated that Huh7 cells are the most sensitive to endosomal
179 escape with mCherry-GAL9 puncta induction from 0.02 $\mu\text{g}/\text{ml}$ and an EC_{50} of 0.1 $\mu\text{g}/\text{ml}$, ~2-4 fold
180 lower than other cell lines (Supplementary Table 1). The correlation between Cy5-mRNA puncta and
181 mCherry-GAL9 structures (Fig. 3f) were explored using linear regression, revealing differences
182 between cell lines both with respect to slope and goodness of fit ($R^2 = 0.573\text{-}0.9188$), indicating that
183 multiple factors likely exist in relating the level of endosomal escape to particle uptake (Fig. 3f,
184 Supplementary Table 1). In general, liver cell lines tended to evoke higher endosomal escape for
185 similar levels of MC3-LNP uptake (Fig. 3f). Comparison of MC3-LNP uptake to dose demonstrated less
186 obvious differences between cell lines (Supplementary Fig. 4b), however, liver cell lines exhibit lower
187 EC_{50} values than the other reporter lines and this may indicate higher efficiency MC3-LNP uptake at
188 lower particle concentrations (Supplementary Table 1), possibly driven by receptor-mediated
189 endocytosis³².

190 Huh7, HepG2 and HeLa cells have very high levels of transfection in response to MC3-LNPs, while
191 NCI-H358 cells had notably fewer EGFP positive cells (~50% at 0.2 $\mu\text{g}/\text{ml}$). NCI-H358 cells tend to

192 grow in clusters in standard culture conditions and we observed that the outer 'edge' cells, had a
193 higher LNP uptake, significant relocalisation of mCherry-GAL9 to punctate structures, and therefore
194 preferentially expressed EGFP (Fig. 3g). By contrast the MC3-LNPs appeared incapable with respect
195 to transfecting NCI-H358 cells in the 'core' of the cluster. This result importantly shows that the
196 mCherry-GAL9 recruitment assay selectively identifies individual cells undergoing endosomal escape
197 and delivery of mRNA to the cytosol for translation, enabling analysis of cell-to-cell variation.

198 We next explored the use of small molecule kinase inhibitors targeting mTOR, a well-established
199 regulatory kinase of protein synthesis, cellular growth and a negative regulator of autophagy³³. We
200 wanted to validate that manipulating cellular translation rate would also impact upon exogenous
201 mRNA translation delivered by LNPs, verifying that our reporter line can demonstrate differences
202 affecting the cellular translation rate. However, macroautophagy induced by mTOR inhibition or
203 stress responses could potentially deliver cytosolic material such as our reporter to the lysosome,
204 leading to a false positive signal³³. We found no significant formation of mCherry-GAL9 structures
205 upon induction of autophagy using the well-characterised dual mTOR complex (mTORC1/2)
206 inhibitors, Torin1 and KU0063794 (Supplementary Fig. 5a-c) indicating autophagy induction does not
207 lead to a false positive signal^{34,35}.

208 Co-incubation of MC3-LNPs with Torin1, KU0063794 or the mTORC1 inhibitor rapamycin led to a
209 reduction in EGFP expression in Huh7 cells, without visibly altering Cy5-mRNA uptake or
210 mCherry-GAL9 recruitment (Supplementary Fig. 6a). Quantification revealed up to a 60% reduction in
211 EGFP translation with Torin1 treatment compared to vehicle controls, while no significant change is
212 seen in particle uptake or endosomal escape indicating the difference is due to reduced mRNA
213 translation (Fig. 3h). This reduction is observed across all mTOR inhibitors at a dose range of
214 50nM-1µM (Supplementary Fig. 6b). Importantly, this confirms that differences in protein translation
215 rate are observable using our mCherry-GAL9 reporter cells and that this can occur independently of
216 endosomal escape.

217 *PNPs induce mCherry-GAL9 recruitment*

218 To demonstrate the broader applicability of the mCherry-GAL9 recruitment assay we examined a
219 different nucleotide delivery system based on an ionisable polymer, comparing a series of
220 compounds formed from DEAEMA (diethylaminoethyl methacrylate) and BMA (butyl methacrylate)
221 and designed to vary in molecular weights but with a maintained ratio of 60:40 of the two moieties,
222 with or without a PEG₂₀₀₀ first block (Fig. 4a)³⁶. The generation and characterisation of this polymer
223 series has recently been reported (currently in submission³⁷). We dosed mCherry-GAL9 HeLa cells
224 with EGFP-encoding mRNA, formulated with the different polymers and thereafter monitored for
225 induction of endosomal escape by recording mCherry-GAL9 relocalisation and EGFP production (Fig.
226 4b,c). The polymers were able to induce mCherry-GAL9 relocalisation, but the response decreased
227 with increasing molecular weight (Fig. 4c, upper panel). This correlated with the level of EGFP
228 expression observed (Fig. 4c, lower panel). The introduction of a PEG leader sequence led to a
229 complete block in endosomal escape and a consequent lack of EGFP expression (Fig. 4b,c), suggesting
230 steric hindrance effects. Closer examination showed that for effective PNPs, the mCherry-GAL9
231 structures formed overlap with Cy5-mRNA structures (Fig. 4d), similar to what was observed for LNPs
232 (Fig. 3a). Particles formed from polymers lacking the PEG-moiety were very large in size compared to
233 LNPs, with hydrodynamic diameters of >500nm according to DLS measurements (Supplementary
234 Table 2). The large particle size led to relatively few particles being taken up per cell, and
235 consequently allowed comparatively simple real-time imaging of the intracellular trafficking of
236 individual Cy5-mRNA containing structures over time, allowing us to capture single escape events.
237 Capturing the trajectory of one single PNP (Fig. 4e) we observe its uptake into a cell and found that
238 after 15-30 minutes, the Cy5-mRNA puncta became mCherry-GAL9 positive, indicating that
239 endosomal disruption has occurred. After approximately 1 h it was possible to observe EGFP
240 translation and cellular fluorescence, confirming functional delivery and translation of the EGFP
241 mRNA. Therefore, we are remarkably able to resolve mCherry-GAL9 recruitment and mRNA
242 translation down to a single endosomal release event.

243 **Endosomal escape is enhanced when lipid nanoparticles contain β -Sitosterol**
244 Having established the mCherry-GAL9 recruitment assay and characterised its functional response to
245 CADs, LNPs, and PNPs, we returned to investigations of how the lipid composition of LNPs influence
246 their potency. It has been recently shown that MC3-LNPs made with β -sitosterol instead of
247 cholesterol have enhanced functional delivery of luciferase mRNA and it was suggested that this may
248 be related to structural changes that enhance fusogenicity^{12,38}. We therefore compared MC3-LNPs
249 formulated with either cholesterol or β -sitosterol and examined their uptake, ability to induce
250 mCherry-GAL9 recruitment and functional delivery (i.e. EGFP expression) across cell lines.

251 Whilst the uptake of Cy5-mRNA was similar between the two LNP types, the formation of
252 mCherry-GAL9 positive structures and subsequent EGFP expression was markedly increased in all
253 reporter lines following the substitution of cholesterol to β -sitosterol (Fig. 5a). In Huh7, HeLa, and
254 HepG2 cells, the effect was most significant in the lower dose range (0.1-0.5 μ g/ml) because of an
255 eventual saturation of the EGFP translation response, which occurred at much lower concentrations
256 for β -sitosterol compared to cholesterol MC3-LNPs (e.g. 0.3 μ g/ml vs 1 μ g/ml in HeLa cells) (Fig. 5b).
257 For NCI-H358 cells, the positive effect of β -sitosterol was observed across the full dose range
258 (Fig. 5b). We used time course analysis over a period of 0-14 h to reveal differences in the kinetics of
259 Cy5-mRNA uptake, mCherry-GAL9 recruitment and EGFP expression between cholesterol and
260 β -sitosterol MC3-LNPs delivered at a dose of 0.1 μ g/ml (Huh7, HeLa, HepG2) or 1 μ g/ml (NCI-H358)
261 (Fig. 5c). Significant differences in the number of mCherry-GAL9 structures formed were observed in
262 all cell lines, occurring from 3 h post-exposure, with concomitant differences in the resulting EGFP
263 expression observable from ~6 h onwards (Fig. 5c). β -sitosterol induced mCherry-GAL9 structures
264 across a longer time period than cholesterol particles (HeLa/HepG2: β -sitosterol plateau at 8 h,
265 cholesterol at 3 h). Higher doses of LNPs (1 μ g/ml) resulted in that the mCherry-GAL9 response
266 equalised in Huh7, HeLa and HepG2 cells and this in turn yielded similar EGFP production
267 (Supplementary Fig. 7). NCI-H358 cells, however, still benefit from the substitution to β -sitosterol at
268 the highest dose of 1.5 μ g/ml. Plotting the number of Cy5-mRNA structures against mCherry-GAL9

269 structures across doses in NCI-H358 cells confirms that β -sitosterol induces higher quantities of
270 endosomal escape for the same level of uptake (Fig. 5d), consistent with their suggested increased
271 fusogenicity¹².

272 Taken together, these data show that LNP variants can have very similar levels of uptake, yet the
273 levels of endosomal escape that the LNPs elicit inside of cells can function independently of uptake,
274 leading to differences in subsequent mRNA delivery and protein translation.

275 *Integration of the mCherry-GAL9 reporter lines into an LNP formulation screening* 276 *platform*

277 Throughout this study we have utilised MC3:Cholesterol:DSPC:DMPE-PEG LNPs to deliver mRNA. This
278 LNP formulation is well-characterised and performs well *in vitro* and *in vivo* and is a suitable tool
279 delivery vehicle to evaluate new assay systems^{6,9}. However, identification of novel particle
280 formulations that outperform this benchmark are needed for broad applicability of mRNA
281 therapeutics *in vivo*. We set up a screening platform, integrating the use of a robotic LNP formulation
282 method, high-throughput particle characterisation (to obtain LNP size and encapsulation efficiency)
283 with automated dosing of reporter cells for live cell imaging on the same Yokogawa spinning disc
284 system that was used earlier (Fig. 6a). As a proof of concept we generated a panel of 72 LNP
285 formulations, containing one of three ionisable lipids (DLin-DMA, DLin-KC2-DMA, DLin-MC3-DMA –
286 hereafter denoted DMA/KC2/MC3)^{39,40}, four phospholipids (DSPC, DOPC, DSPE, DOPE), three sterols
287 (Cholesterol, 7 β -Hydroxycholesterol, 25-Hydroxycholesterol – hereafter 7B-HC/25-HC), and two PEG-
288 lipids (DMPE-PEG, DMG-PEG) (Supplementary Fig. 8a), including the standard MC3-LNP formulation
289 that has been used throughout this work.

290 The LNPs formed with the robotic system were larger at 150-400 nm (Supplementary Fig. 8b),
291 compared to the LNPs used in previous experiments (which were formulated using a microfluidic
292 device). Their size was determined using a DLS plate reader with 90° scattering angle, which may
293 overstate actual particle size⁴¹; control measurement of the size of some of the LNPs using a Malvern
294 Zetasizer cuvette-based instrument with a back-scatter angle of 173° yielded z-average sizes ~25%

295 smaller (Supplementary Fig. 8c) confirming this view, but LNPs were nevertheless larger than those
296 formed using the NanoAssemblr. In addition, robotic LNP formulation resulted in poorer mRNA
297 encapsulation (30-60%) than NanoAssemblr formed particles (~95-99%) (Supplementary Fig. 8b).

298 Using this screening platform, we exposed mCherry-GAL9 Huh7 cells to LNPs and monitored particle
299 uptake, mCherry-GAL9 recruitment, EGFP expression and percentage of cellular transfection by time-
300 lapse microscopy as carried out earlier (Fig. 3d). To allow easier comparison between LNP
301 formulations, a heatmap was generated to represent the response of each assayed parameter (Cy5
302 uptake, GAL9 recruitment, EGFP expression, percent transfection) at 14 h post-dosing (Fig. 6b).

303 In this screen, we explored different cholesterol derivatives, expanding the analysis of β -sitosterol
304 (Fig. 5). We substituted cholesterol to 7B-HC or 25-HC, a hydroxyl modification of cholesterol ring B
305 or the tail region respectively. The characteristics of the 7B-HC LNPs were similar to cholesterol LNPs,
306 however, 25-HC particles suffered from much lower encapsulation efficiencies (average 29% v 43%,
307 Fig. 6c – left panel). The cellular uptake of 7B-HC and 25-HC particles was severely ablated (Fig. 6b,c).
308 Despite this, there was still recruitment of mCherry-GAL9, but interestingly this did not result in
309 functional mRNA delivery, as evidenced by the near lack of EGFP expression and low transfection
310 level. This suggests that even if endosome damage is key for the release of mRNA from endosomes,
311 additional parameters effect to what extent the delivered mRNA can be utilised by the cell; inclusion
312 of 7B-HC or 25-HC into the LNPs appear to hinder protein translation. Subsequent data comparisons,
313 for this reason, focus solely upon LNPs containing cholesterol.

314 DMA and KC2 are ionisable lipids that have similar pKas of 6.7 and 6.8 respectively (~6.44 for MC3)
315 but have been reported to have ~20-fold range in potency in mice as determined by Factor VII ED₅₀
316 (1mg/kg (DMA) v 0.1 mg/kg (KC2) 0.05mg/kg (MC3))^{9,40}. Consistent with this, the substitution of MC3
317 to DMA or KC2 led to reduced particle uptake, reduced levels of endosomal escape and consequently
318 markedly reduced levels of EGFP expression (Fig. 6b,d). However, KC2 and DMA LNPs, whilst resulting
319 in similar levels of uptake, perform differently with respect to their capacity to induce endosome

320 damage (Fig. 6d), with KC2 having enhanced endosomal escape potency and thereby outperforming
321 DMA in terms of functional delivery (protein expression) and transfection efficiency.

322 Finally, we examined differences in particles containing either DMG-PEG or DMPE-PEG. Whilst both
323 contain a C14-acyl chain and PEG₂₀₀₀, DMPE contains a phosphate group giving the overall molecule a
324 negative charge compared to DMG that is neutral. Substitution to DMG-PEG resulted in reduced
325 uptake and slower kinetics, lower endosomal escape rates and ultimately impaired EGFP production
326 across all particles surveyed (Fig. 6b,e). It has been shown that the half-life of DMPE-PEG on
327 nanoparticle surfaces is shorter than DMG-PEG¹³ and this may account for some of the changes
328 observed. Additionally, the particle charge difference may also lead to differences in interactions
329 with serum proteins that are important for cellular uptake and/or endosomal escape¹³ or with the
330 endosomal membrane. Representative microscopy images demonstrating changes to key particle
331 components on the uptake, GAL9 recruitment and EGFP translation are shown in Supplementary Fig.
332 9.

333 Altogether, the screen presented in Fig. 6 illustrates that LNPs with similar physical properties such as
334 size, PDI and encapsulation but formed from different lipids can demonstrate great variation in terms
335 of how they are taken up by cells and are able to deliver mRNA. Integration of the mCherry-GAL9
336 reporter into a screening platform with multiple cellular read-outs have allowed us to probe in
337 greater detail to which delivery step a certain lipid alteration can modulate LNP potency and
338 highlights the benefits of utilising such a reporter system for deriving greater insights into
339 nanoparticle function.

340 DISCUSSION

341 In this work we have, for the first time, demonstrated a comprehensive system for the monitoring of
342 nanoparticle trafficking from uptake, through to endosomal escape, and to protein translation within
343 a single microscopy assay and established a screening platform by integrating the assay with robotic
344 formulation and high-throughput biophysical analysis of LNPs.

345 The benefits of such an assay are clear in that they allow comparison of nanoparticles across multiple
346 relevant parameters to ascertain mechanistically why one particle formulation may outperform
347 another, an explanation that is often absent if simply looking at protein translation. By automated
348 formulation of a panel of 72 LNPs, we were able to examine the relative differences of substitution of
349 each lipid component. This approach can highlight the general effect of component substitution but
350 reduces the reliance on using a single LNP to make the decision of efficacy. Our results indicated that
351 a particle formulated using DLin-MC3-DMA, Cholesterol, and DMPE-PEG would perform best across
352 uptake and endosomal escape parameters. Indeed, particles comprised of these three components
353 and a variable phospholipid were the highest performing particles in our screen. Whilst this
354 replicates our current understanding of well performing LNP formulation, our study importantly
355 demonstrates and validates that this assay can be used to survey a wider chemical space of poorly
356 explored lipids, with a rich information read-out. This will make it possible to identify LNP
357 formulations that outperform benchmark LNPs or can achieve the same level of delivery at lower
358 dosing requirements.

359 Our analysis of substitution of cholesterol to β -sitosterol within LNPs confirms that particle uptake
360 and endosomal escape can act independently of one another and highlights the importance of
361 understanding and optimising both parameters during the design of next-generation LNPs. Cellular
362 uptake of these particles was similar but endosomal escape was strongly improved by switching to
363 β -Sitosterol, consistent with a recent report that β -sitosterol particles have a multi-faceted structure
364 that may directly modulate endosomal fusion³⁸. Even so, little is known about if there are
365 fundamental underlying differences in the endosomal compartments that particles are taken up in or

366 whether there are other differences in the protein corona that forms prior to uptake that may alter
367 particle fusion/endosomal escape properties. Interestingly, substitution to β -sitosterol did not
368 significantly increase the maximum amount of EGFP protein attainable suggesting natural limits exist
369 on how much exogenous mRNA can be utilised by cells. Further benefits from mRNA therapies may
370 therefore be obtainable by modulating cellular translation rates or modifying mRNA cargo sequence
371 to enhance ribosome docking and translation. The relative benefit of achieving enhanced endosomal
372 escape may therefore not necessarily be through higher protein expression, instead the benefits may
373 come from being able to reduce dosing requirements and hence reduce the cost of mRNA therapies
374 and the risk of toxic side-effects, in particular from the drug vehicle itself.

375 We were also able to induce a GAL9 response without a delivery vehicle, but using small molecule
376 endosomolytic drugs such as UNC2383. The response of the small molecules appeared
377 phenotypically similar to that induced by LNPs or PNPs and is consistent with the compounds
378 proven capability to delivery naked oligonucleotides ²⁷. However, the cellular toxicity associated with
379 these compounds tentatively suggests underlying differences in the process inducing GAL9
380 recruitment and may hint at a more severe endolysosomal damaging approach rather than the fusion
381 that is anticipated with ionisable LNPs. Variation in the size of the mCherry-GAL9 structures
382 generated by UNC and chloroquine suggests underlying differences in the endolysosome membrane
383 compartments targeted by CADs, this may correspond with differences in utility for aiding
384 oligonucleotide delivery. Future studies are required to determine whether combining small
385 molecules with LNPs/PNPs is a viable strategy to enhance cellular delivery of mRNA, as previously
386 shown with small oligonucleotides. Recent work has suggested that some CADs are able to induce
387 endosomal rupture and enhance nanoparticle-mediated delivery, but this is dependent upon
388 nanoparticle composition ⁴². In addition, the rapid and acute onset of GAL9 recruitment with UNC
389 compounds suggests accurately synchronising compound dosing with particle uptake is likely to be
390 critical. We have shown that mCherry-GAL9 cellular models have a large signal window between the
391 minimum and maximum responses (and therefore a high Z' factor), making this assay amenable for

392 subsequent high-content screening for novel small molecules or LNPs that are potent inducers of
393 endosomal rupture and that will allow us to explore this point further.

394 Not all delivery vehicles induce Galectin recruitment responses. Recently, extracellular vehicles were
395 demonstrated to act in a GAL3-independent manner, however, it should be noted that GAL3 is a
396 weaker identifier of endosomal damage than GAL9^{22,43}. It will be interesting to examine whether
397 other emerging delivery vectors for oligonucleotides such as dendrimers, particle modifications with
398 cell-penetrating peptides or the use of viral-like particles invoke GAL9 recruitment responses that are
399 similar to those induced by LNPs. Currently, readout of endosomal escape with mCherry-GAL9
400 recruitment corresponds strongly with the translation of cargo mRNA and is therefore an excellent
401 predictor for nanoparticle efficacy. However, we demonstrate GAL9 recruitment is not always
402 indicative of successful protein production as translation can still be decoupled from endosomal
403 escape as demonstrated by the utilisation of mTOR inhibitors or the substitution of cholesterol for
404 7B-HC/25-HC in LNPs. Hydroxycholesterols have previously been shown to inhibit mTOR signalling
405 and therefore protein translation⁴⁴, but could also potentially influence mRNA-lipid complexation
406 and hinder cytosolic mRNA release.

407 Interestingly, by integrating the mCherry-Gal9 reporter into multiple cell lines, we can also begin to
408 explore cell to cell differences in response to LNPs. Our study showed that liver-derived cell models
409 demonstrated greater sensitivity to endosomal disruption from MC3-LNPs than non-liver cell models
410 without equivalent differences in the level of particle uptake, providing a more detailed
411 understanding to the observation by Sayers et al. that LNPs are differently effective in liver-derived
412 Huh7 compared to lung-derived NCI-H358⁴⁵. Examination of a wider range of LNP formulations and
413 cationic lipids will be important to determine whether this is an intrinsic sensitivity of these cell
414 models to nanoparticle delivery or whether this is indicative of a composition-driven LNP selectivity
415 for certain cell types. Similarly, integrating the mCherry-GAL9 into a broader range of cellular models
416 will be important for screening particle formulations for identification of parameters important for
417 selective uptake to ultimately facilitate selective organ targeting *in vivo*.

418 By improving our understanding of LNP characteristics that are critical to achieve particle uptake and
419 endosomal escape across cellular models, we can ideally achieve therapeutic doses using lower
420 amounts of potentially immunogenic lipid carriers and reduce the costs for future potential
421 treatments. Identification of novel particle formulations will undoubtedly require significant efforts
422 to screen nanoparticle variations in a robust manner, we believe this assay forms a fundamental
423 basis for future screening endeavours to progress the development of drug delivery systems.

424 ACKNOWLEDGEMENTS

425 M.J.M and A.M.S are PostDoc fellows of the AstraZeneca R&D PostDoc Program. G.O is a member of
426 the AstraZeneca R&D graduate programme. This work was conducted within the Industrial Research
427 Centre, FoRmulaEx–Nucleotide Functional Drug Delivery, and with associated financial support to
428 E.K.E from the Swedish Foundation for Strategic Research (SSF, grant No. IRC15-0065). We thank Erik
429 Oude Blenke for the formulation of β -sitosterol containing LNPs.

430 AUTHOR CONTRIBUTIONS

431 M.J.M and G.O performed experiments, study design and critical discussions were carried out
432 between M.J.M, G.O, A.C, E.K.E and A.S. PCR was carried out by A.M.S, western blots by E.L.I and
433 FACS of reporter lines was performed by A.G. The manuscript was written by M.J.M, E.K.E and A.S
434 with input from all authors.

435 DATA AVAILABILITY

436 The source data underlying all quantitative figures are provided as a Source Data file. All data
437 supporting the findings of this study is available from the corresponding author upon reasonable
438 request.

439 COMPETING INTERESTS

440 M.J.M, G.O, A.M.S, E.L.I, A.G, A.C and A.S are or were employees of AstraZeneca plc

441 METHODS

442 Materials

443 Cholesterol (C8667), DOPC (P6354) and Chloroquine (C6628) were obtained from Sigma Aldrich.
444 DSPC (LP-R4-076), DOPE (LP-R4-069) were from Merck-Millipore. 7 β -hydroxycholesterol (700035P),
445 25-hydroxycholesterol (700019P), β -sitosterol (700095P) and DSPE (850715P) were from Avanti Polar
446 Lipids. DMG-PEG₂₀₀₀ (GM-020) and DMPE-PEG₂₀₀₀ (PM-020CN) were from Nof America Corporation.
447 Cationic lipids DLin-DMA, DLin-KC2-DMA, DLin-MC3-DMA and small molecules KU0063794,
448 Rapamycin, Torin1, UNC2383, UNC4167, UNC10217938A were chemically synthesised.

449 Cell Line Maintenance & Generation of GAL9 Reporter

450 HeLa (CCL-2), HepG2 (HB-6065) and NCI-H358 (CRL-5807) cells were purchased from ATCC whilst
451 Huh7 (Riken - RCB1366) were a kind gift from Prof. Samir El-Andalousi (KI, Stockholm), all cell lines
452 were authenticated by STR profiling. Cells were maintained at 37°C in a humidified incubator in a
453 complete media of DMEM + Glutamax (Huh7, HeLa, HepG2) or RPMI + Glutamax (NCI-H358 cells)
454 both supplemented with 10% foetal bovine serum.

455 Stable cells expressing mCherry-GAL9 were generated by knock-in at the *AAVS1* locus. Cells were
456 seeded at 2x10⁵ cells/well (12-well) and transfected with mCherry-GAL9 reporter:AAVS1 zinc-finger
457 nuclease (1:9) using FuGENE HD transfection reagent (Promega) as per manufacturer's instructions.
458 Cells were incubated for 48 h before addition of 1 μ g/ml Puromycin to select for stably integrated
459 cells.

460 Imaging experiments and quantitation

461 Cells were seeded into 384-well CellCarrier Ultra plates (PerkinElmer: 6007558) in complete media a
462 minimum of 16 h prior to treatment. Hoechst 33342 was added to cell culture medium at 0.5 μ g/ml a
463 minimum of 1 h prior to imaging experiments to evenly stain nuclei prior to experiment start points.
464 Nanoparticle or small molecules were first dispensed into a 384-well source plate (Greiner: 781280)

465 containing appropriate complete media + 0.5 µg/ml Hoechst by using an Echo 655T acoustic
466 dispenser (Labcyte). At the experimental start point, the media on cells was removed and replaced
467 directly by media containing LNPs/small molecules from the source plate using a Bravo liquid
468 handling robot (Agilent). The cell plate was then moved to the microscope and imaged immediately.
469 Live-cell experiments were carried out within a humidified imaging chamber maintained at 5% CO₂
470 with a CV7000 (Yokogawa) spinning disk confocal microscope utilising a 20x objective (NA 0.75).
471 Images were obtained using a 445nm laser (BP445/45nm), 488nm laser (BP522/35), 561nm laser
472 (BP600/37) or 640nm laser (BP676/29) for relevant fluorophores. For microscopy time-course
473 measurements, the same fields of view were imaged over time that had received the experimental
474 treatment noted in the figure. Images were processed and analysed for relevant features and
475 parameters indicated in figures utilising Columbus image-analysis software (Perkin Elmer, v2.9.0).
476 Data was exported and handled in Spotfire (Tibco, v10.3), in many cases numerical values obtained
477 were normalised for combining between experimental replicates. Data was exported and plotted
478 with Prism (Graphpad, v8.0.1).

479 **Statistics and Significance**

480 Statistical testing was carried out in Prism with relevant multiple comparisons and post-test where
481 appropriate, see figure legends for tests applied.

482 **PCR and droplet digital PCR**

483 DNA was extracted from wild-type (WT) and GAL9 transgenic cells pools using QuickExtract™ DNA
484 extraction solution (Lucigen), according to the manufacturer's instructions. Briefly, extraction
485 solution was added to cell pellets, followed by samples vortexing and incubation at 65 °C for 6 min.
486 Samples were vortexed again and incubated at 98 °C for 2 min. For ddPCR, the same amount of DNA
487 (50 ng) for all samples was mixed with ddPCR supermix for probes, puromycin-FAM primers/probe
488 mix, AP3B1-HEX primers/probe mix (all from Bio-Rad), and Hind III 5U (New England BioLabs Inc.)
489 restriction enzyme. Samples were incubated for 10 min at room temperature (RT) for DNA

490 fragmentation. PCR droplets were generated on an Automatic Droplet Generator using oil for probes
491 (all from Bio-Rad). Target genes were amplified on a C1000 thermal cycler (Bio-Rad) according to the
492 following conditions: 95 °C for 10 min, followed by 40 cycles of template denaturation at 94 °C for 30
493 sec, and annealing and extension at 57 °C for 1 min, with a temperature ramping ratio of 2 °C/sec,
494 with a final incubation step at 98 °C for 10 min. PCR droplets were analysed on a QX200 droplet
495 reader equipped with QuantaSoft software v.1.7.4 (Bio-Rad). Populations of fluorescent droplets
496 were identified as depicted in Supplementary Fig. 1 and the average copy number of target gene
497 insertions per cell was calculated using the Copy Number Variation algorithm, considering a 2x ploidy
498 for HepG2 and Huh7 cell lines, and a 3x ploidy for HeLa and NCI-H358 cell lines, and normalised to
499 the copy number of the reference gene AP3B1 . For endpoint PCR, DNA was first further purified by
500 mixing with ice-cold ethanol 99,9% in a ratio 1:3 (v/v), followed by overnight incubation at -20 °C, and
501 then by washing with ethanol 70%. Samples were dried at RT and DNA dissolved in nuclease-free
502 water. Purified DNA (100 ng) was then mixed with Phusion Flash PCR master mix (ThermoFisher
503 Scientific) and primers spanning the AAVS1 locus and the donor construct, followed by incubation on
504 a C1000 thermal cycler (Bio-Rad) according to the following conditions: 98 °C for 10 sec, followed by
505 35 cycles of template denaturation at 98 °C for 1 sec, annealing at 54 °C for 5 sec and extension at 72
506 °C for 15 sec, with a final incubation step at 72 °C for 1 min. Amplicons were then resolved in a 2%
507 agarose E-gel, using TrackiT 1 Kb plus DNA ladder (all from ThermoFisher Scientific), followed by gel
508 imaging on a Gel-Doc system (Bio-Rad).

509 Fluorescence-activated cell sorting (FACS)

510 WT and mCherry-GAL9 reporter cells were grown and expanded until 80% confluency. Cells were
511 washed twice with PBS, detached with TrypLE Express (10 min, 37°C), resuspended in FACS buffer
512 (5% FBS in PBS) and filtered in FACS tubes using a 35 µm mesh (Falcon). Cell sorting was performed
513 on a FACSAria™ III cytometer (from BD Instrument), using the BD FACSDiva Software. For each cell
514 type, WT cells were used to set up the voltage of the Forward Scatter (FSC) and Side Scatter (SSC) as

515 well as to adjust the autofluorescence level in the mCherry channel. Debris were excluded by plotting
516 the FSC vs SSC with all events and gating for living cells, and cell aggregates (doublets/clusters) were
517 excluded by plotting the SSC-height vs SSC-area with living cells and gating for single cells. mCherry-
518 positive GAL9 reporter cells were sorted in bulk according to two fluorescence intensity levels.
519 Following sorting, cells were spun down (200 g, 5 min at RT) to remove excess FACS buffer and then
520 grown for a week in presence of 1% penicillin-streptomycin. Antibiotics-free culture medium was
521 used for cell experiments.

522 Western Blotting

523 Cell pellets (5×10^6 cells) were lysed in RIPA buffer (Thermo Fisher Scientific) supplemented with
524 protease inhibitors (Sigma-Aldrich) for 15 minutes on ice. Total protein content was determined using
525 the Qubit protein assay kit (Thermo Fisher Scientific) following the manufacturer's protocol. Protein
526 lyses (40 μ g/lane) were separated by SDS-PAGE and transferred to polyvinylidene fluoride membranes
527 (BioRad). Membranes were blocked with Intercept (TBS) blocking buffer (LI-COR) for 1 h at RT and
528 incubated with primary antibodies mCherry (E5DF8, #43590) and β -Tubulin (9F3, #2128) (Cell Signalling
529 Technologies) diluted 1:1000 in blocking buffer at 4°C overnight. Membranes were washed three times
530 with 0.1 % TBS-Tween and incubated for 1 h at RT with IRDye 800CW goat anti-rabbit IgG cat# 926-
531 32211 (LI-COR) diluted 1:20,000 in 0.1 % TBS-Tween. Following washes, membranes were visualized
532 with the Odyssey CLx imaging system and processed in Image Studio (v4.0, LI-COR).

533 Formation of LNPs (NanoAssemblr)

534 DLin-MC3-DMA cholesterol or β -sitosterol containing lipid nanoparticles were formulated using a
535 NanoAssemblr (Precision NanoSystems) by microfluidic mixing chip. Briefly, lipids were prepared in
536 Ethanol at a ratio of 50:38.5:10:1.5 (MC3:Sterol:DSPC:DMPE-PEG2000) at a 10:1 (w/w) Lipid:mRNA
537 cargo, N:P ratio = \sim 3:1. mRNA cargo encoding for EGFP was prepared at a 4:1 ratio (Unlabelled:Cy5
538 labelled – TriLink: L7201/7701) in 50 mM Citrate pH 3 buffer (TekNova: Q2445). Lipid and mRNA
539 containing solutions were mixed 3:1 (Citrate:Ethanol) at a constant flow rate of 12 ml/min to form

540 nanoparticles. Particles were dialysed overnight into PBS pH 7.4 at 4 °C and sterile filtered using a
541 0.23µm filter. Characteristics of LNP batches used in this study are shown in Supplementary Table 2

542 **Formation of LNPs (Automated Pipetting)**

543 Robotic formulation of particles was achieved utilising a Bravo liquid handling robot utilising VWorks
544 software (v12.2.0.1306, Agilent). Particles were prepared at a ratio of 50:38.5:10:1.5 (Cationic
545 Lipid:Sterol:Phospholipid:PEG-Lipid) at a 20:1 (w/w) lipid:mRNA cargo, N:P ratio = ~6:1. 7.5 µl of each
546 lipid component was combined per well to a final volume of 30 µl. mRNA cargo encoding for EGFP
547 was prepared at a 4:1 ratio (Unlabelled: Cy5 labelled – TriLink: L7201/7701) in 50 mM Citrate pH 3
548 buffer (TekNova: Q2445) at 30µl per well (122 µg/ml). 10 µl of the lipid-ethanol mix was added
549 directly to mRNA mix and pipetted up and down 10 x 20 µl. An equal volume (40 µl) of PBS pH 7.4
550 was then added to the mRNA/lipid and mixed a further 5x 20 µl and then incubated at 4 °C overnight
551 prior to usage.

552 **Formation of PNPs (Automated Pipetting)**

553 Polyplexes were prepared utilising a Bravo robot as for LNPs (above). 20 µL of 50 mM citrate pH 3
554 (TekNova #Q2445) buffered mRNA (4:1 GFP: Cy5 – TriLink CleanCap mRNA L-7201/L-7701) (100 µg/ml)
555 was injected into wells (Greiner V-bottom #781280) that contain 20 µL of the desired polymer
556 solution at an amine:phosphate ratio of 8:1 assuming 50% amines charged per polymer. After
557 addition of the RNA solution, polyplex suspensions were mixed through 10 x 15µl mix steps and
558 incubated at RT for 30 mins prior to addition of an equal volume (40µl) 1M Tris-HCl pH 8 (TekNova
559 #T1080). Polyplexes were mixed 5 x 15 µl before moving to 4 °C for 16 hours prior to use.

560 **Particle Characterisation – DLS and Encapsulation**

561 Size (Diameter, Z average) of particles and polydispersity index (PDI) was determined by dynamic
562 light scattering utilising a Malvern Zetasizer ($\lambda = 633$ nm, scattering angle = 173°) for particles formed
563 by NanoAssemblr or a Malvern Zetasizer APS ($\lambda = 832$ nm, scattering angle = 90°) for particles
564 formed by pipetting. In both cases standard viscosity and refractive index values for pure water at

565 25 °C, 0.8872 mPa and 1.33 respectively, were used for data analysis within Zetasizer software
566 (v7.12).

567 Ribogreen dye (Thermo Fisher Scientific) was used according to manufacturer's guidelines \pm 1%

568 Triton to ascertain encapsulated mRNA by comparison to a relevant mRNA standard curve.

569 References

- 570 1. Stein, C. A. & Castanotto, D. FDA-Approved Oligonucleotide Therapies in 2017. *Mol. Ther.* **25**,
571 1069–1075 (2017).
- 572 2. Valeur, E. *et al.* New Modalities for Challenging Targets in Drug Discovery. *Angew. Chemie -*
573 *Int. Ed.* **56**, 10294–10323 (2017).
- 574 3. Dowdy, S. F. Overcoming cellular barriers for RNA therapeutics. *Nat. Biotechnol.* **35**, 222–229
575 (2017).
- 576 4. Kauffman, K. J., Webber, M. J. & Anderson, D. G. Materials for non-viral intracellular delivery
577 of messenger RNA therapeutics. *J. Control. Release* **240**, 227–234 (2016).
- 578 5. Kaczmarek, J. C., Kowalski, P. S. & Anderson, D. G. Advances in the delivery of RNA
579 therapeutics: From concept to clinical reality. *Genome Med.* **9**, 1–16 (2017).
- 580 6. Gilleron, J. *et al.* Image-based analysis of lipid nanoparticle-mediated siRNA delivery,
581 intracellular trafficking and endosomal escape. *Nat. Biotechnol.* **31**, 638–46 (2013).
- 582 7. Wittrup, A. *et al.* Visualizing lipid-formulated siRNA release from endosomes and target gene
583 knockdown. *Nat. Biotechnol.* **33**, 870–6 (2015).
- 584 8. Yonezawa, S., Koide, H. & Asai, T. Recent advances in siRNA delivery mediated by lipid-based
585 nanoparticles. *Adv. Drug Deliv. Rev.* (2020). doi:10.1016/j.addr.2020.07.022
- 586 9. Jayaraman, M. *et al.* Maximizing the potency of siRNA lipid nanoparticles for hepatic gene
587 silencing in vivo. *Angew. Chem. Int. Ed. Engl.* **51**, 8529–33 (2012).
- 588 10. Whitehead, K. A. *et al.* Degradable lipid nanoparticles with predictable in vivo siRNA delivery
589 activity. *Nat. Commun.* **5**, 1–10 (2014).
- 590 11. Paunovska, K. *et al.* Nanoparticles Containing Oxidized Cholesterol Deliver mRNA to the Liver
591 Microenvironment at Clinically Relevant Doses. *Adv. Mater.* **31**, e1807748 (2019).

- 592 12. Patel, S. *et al.* Naturally-occurring cholesterol analogues in lipid nanoparticles induce
593 polymorphic shape and enhance intracellular delivery of mRNA. *Nat. Commun.* **11**, 983 (2020).
- 594 13. Zhu, X. *et al.* Surface de-PEGylation controls nanoparticle-mediated siRNA delivery in vitro and
595 in vivo. *Theranostics* **7**, 1990–2002 (2017).
- 596 14. Chen, D., Parayath, N., Ganesh, S., Wang, W. & Amiji, M. The role of apolipoprotein- And
597 vitronectin-enriched protein corona on lipid nanoparticles for- And vivo targeted delivery and
598 transfection of oligonucleotides in murine tumor models. *Nanoscale* **11**, 18806–18824 (2019).
- 599 15. Kauffman, K. J. *et al.* Optimization of Lipid Nanoparticle Formulations for mRNA Delivery in
600 Vivo with Fractional Factorial and Definitive Screening Designs. *Nano Lett.* **15**, 7300–7306
601 (2015).
- 602 16. Smith, S. A., Selby, L. I., Johnston, A. P. R. & Such, G. K. The Endosomal Escape of
603 Nanoparticles: Toward More Efficient Cellular Delivery. *Bioconjug. Chem.* **30**, 263–272 (2019).
- 604 17. Barondes, S. H. *et al.* Galectins: A family of animal β -galactoside-binding lectins. *Cell* **76**, 597–
605 598 (1994).
- 606 18. Paz, I. *et al.* Galectin-3, a marker for vacuole lysis by invasive pathogens. *Cell. Microbiol.* **12**,
607 530–544 (2010).
- 608 19. Maier, O., Marvin, S. A., Wodrich, H., Campbell, E. M. & Wiethoff, C. M. Spatiotemporal
609 Dynamics of Adenovirus Membrane Rupture and Endosomal Escape. *J. Virol.* **86**, 10821–10828
610 (2012).
- 611 20. Thurston, T. L. M., Wandel, M. P., von Muhlinen, N., Foeglein, A. & Randow, F. Galectin 8
612 targets damaged vesicles for autophagy to defend cells against bacterial invasion. *Nature* **482**,
613 414–8 (2012).
- 614 21. Kilchrist, K. V. *et al.* Gal8 Visualization of Endosome Disruption Predicts Carrier-Mediated

- 615 Biologic Drug Intracellular Bioavailability. *ACS Nano* **13**, 1136–1152 (2019).
- 616 22. Du Rietz, H., Hedlund, H., Wilhelmson, S., Nordenfelt, P., Wittrup, A. Imaging small molecule-
617 induced endosomal escape of siRNA. *Nat. Commun.* (2020). doi:10.1038/s41467-020-15300-1
- 618 23. Maresca, M., Lin, V. G., Guo, N. & Yang, Y. Obligate ligation-gated recombination (ObLiGaRe):
619 custom-designed nuclease-mediated targeted integration through nonhomologous end
620 joining. *Genome Res.* **23**, 539–46 (2013).
- 621 24. Nishi, N., Itoh, A., Shoji, H., Miyanaka, H. & Nakamura, T. Galectin-8 and galectin-9 are novel
622 substrates for thrombin. *Glycobiology* **16**, 15–20 (2006).
- 623 25. Bänfer, S. & Jacob, R. Galectins in Intra- and Extracellular Vesicles. *Biomolecules* **10**, 1–12
624 (2020).
- 625 26. Maxfield, F. R. Weak bases and ionophores rapidly and reversibly raise the pH of endocytic
626 vesicles in cultured mouse fibroblasts. *J. Cell Biol.* **95**, 676–681 (1982).
- 627 27. Wang, L. *et al.* A Novel Family of Small Molecules that Enhance the Intracellular Delivery and
628 Pharmacological Effectiveness of Antisense and Splice Switching Oligonucleotides. *ACS Chem.*
629 *Biol.* **12**, 1999–2007 (2017).
- 630 28. Yang, B. *et al.* High-throughput screening identifies small molecules that enhance the
631 pharmacological effects of oligonucleotides. *Nucleic Acids Res.* **43**, 1987–96 (2015).
- 632 29. Chen, Z. *et al.* Mitochondrial E3 ligase MARCH5 regulates FUNDC1 to fine-tune hypoxic
633 mitophagy. *EMBO Rep.* **18**, 495–509 (2017).
- 634 30. Hansjosten, I. *et al.* Microscopy-based high-throughput assays enable multi-parametric
635 analysis to assess adverse effects of nanomaterials in various cell lines. *Arch. Toxicol.* **92**, 633–
636 649 (2018).
- 637 31. Iversen, P. W., Eastwood, B. J., Sittampalam, G. S. & Cox, K. L. A comparison of assay

- 638 performance measures in screening assays: Signal window, Z' factor, and assay variability
639 ratio. *J. Biomol. Screen.* **11**, 247–252 (2006).
- 640 32. Akinc, A. *et al.* Targeted delivery of RNAi therapeutics with endogenous and exogenous
641 ligand-based mechanisms. *Mol. Ther.* **18**, 1357–64 (2010).
- 642 33. Liu, G. Y. & Sabatini, D. M. mTOR at the nexus of nutrition, growth, ageing and disease. *Nat.*
643 *Rev. Mol. Cell Biol.* **21**, 183–203 (2020).
- 644 34. Thoreen, C. C. *et al.* An ATP-competitive mammalian target of rapamycin inhibitor reveals
645 rapamycin-resistant functions of mTORC1. *J. Biol. Chem.* **284**, 8023–8032 (2009).
- 646 35. García-Martínez, J. M. *et al.* Ku-0063794 is a specific inhibitor of the mammalian target of
647 rapamycin (mTOR). *Biochem. J.* **421**, 29–42 (2009).
- 648 36. Manganiello, M. J., Cheng, C., Convertine, A. J., Bryers, J. D. & Stayton, P. S. Diblock
649 copolymers with tunable pH transitions for gene delivery. *Biomaterials* **33**, 2301–2309 (2012).
- 650 37. Munson, M. J., Ulkoski, D., Wilson, J., Sabirsh, A. & Krishnamurthy, V. An Automated High-
651 Throughput Study of Endosomolytic Polymers for mRNA delivery. *Manuscr. Prep.*
- 652 38. Eygeris, Y., Patel, S., Jozic, A. & Sahay, G. Deconvoluting Lipid Nanoparticle Structure for
653 Messenger RNA Delivery. *Nano Lett.* [acs.nanolett.0c01386](https://doi.org/10.1021/acs.nanolett.0c01386) (2020).
654 [doi:10.1021/acs.nanolett.0c01386](https://doi.org/10.1021/acs.nanolett.0c01386)
- 655 39. Heyes, J., Palmer, L., Bremner, K. & MacLachlan, I. Cationic lipid saturation influences
656 intracellular delivery of encapsulated nucleic acids. *J. Control. Release* **107**, 276–87 (2005).
- 657 40. Semple, S. C. *et al.* Rational design of cationic lipids for siRNA delivery. *Nat. Biotechnol.* **28**,
658 172–6 (2010).
- 659 41. Stetefeld, J., McKenna, S. A. & Patel, T. R. Dynamic light scattering: a practical guide and
660 applications in biomedical sciences. *Biophys. Rev.* **8**, 409–427 (2016).

- 661 42. Van de Vyver, T. *et al.* Cationic Amphiphilic Drugs Boost the Lysosomal Escape of Small Nucleic
662 Acid Therapeutics in a Nanocarrier-Dependent Manner. *ACS Nano* **14**, 4774–4791 (2020).
- 663 43. Joshi, B. S., de Beer, M. A., Giepmans, B. N. G. & Zuhorn, I. S. Endocytosis of Extracellular
664 Vesicles and Release of Their Cargo from Endosomes. *ACS Nano* **14**, 4444–4455 (2020).
- 665 44. Castellano, B. M. *et al.* Lysosomal cholesterol activates mTORC1 via an SLC38A9-Niemann-Pick
666 C1 signaling complex. *Science* **355**, 1306–1311 (2017).
- 667 45. Sayers, E. J. *et al.* Endocytic Profiling of Cancer Cell Models Reveals Critical Factors Influencing
668 LNP-Mediated mRNA Delivery and Protein Expression. *Mol. Ther.* **27**, 1950–1962 (2019).
- 669

Figures

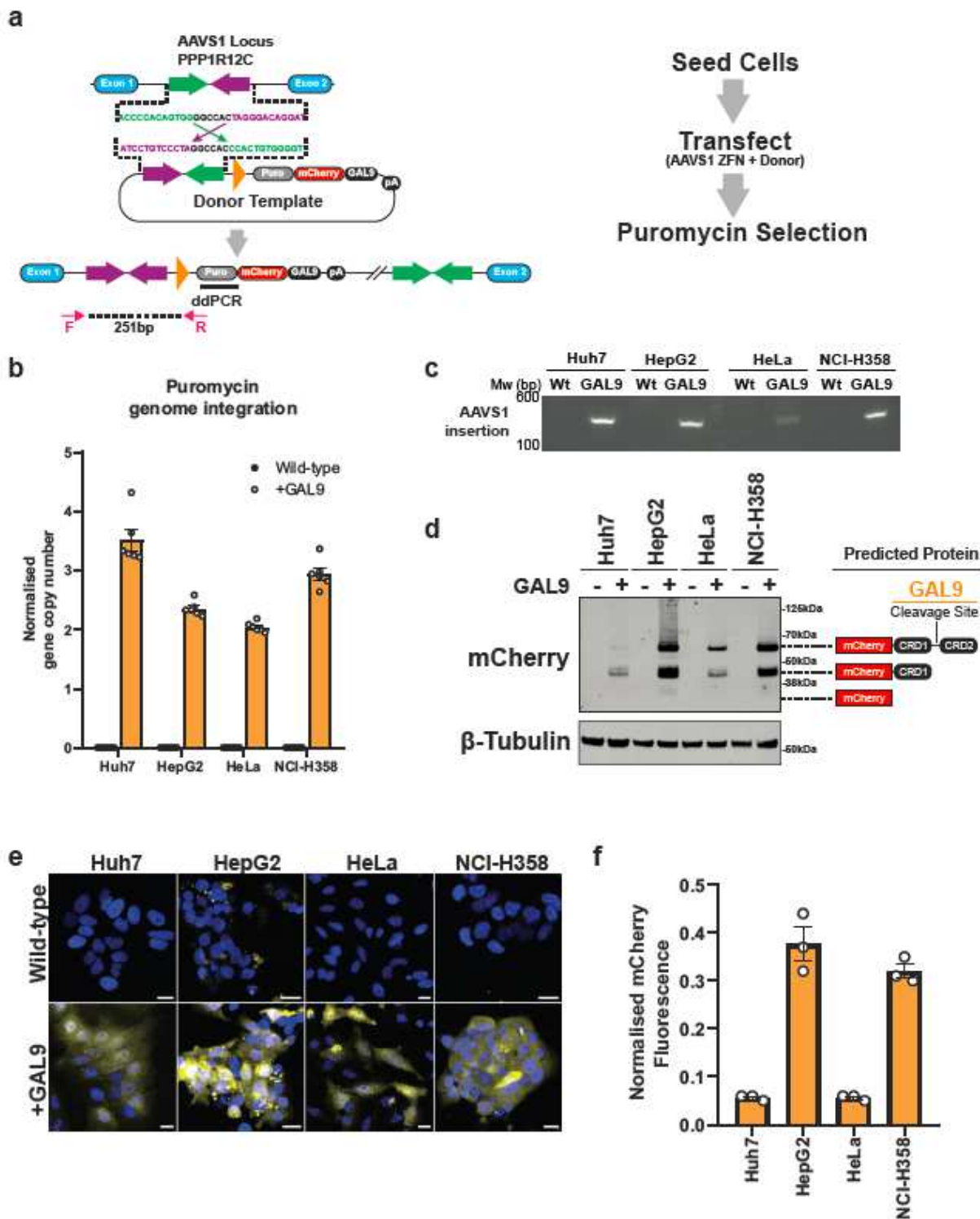


Figure 1

Generation of mCherry-GAL9 knock-in cell lines a Knock-In strategy for mCherry-GAL9. Reporter plasmid contains analogous zinc finger nuclease (ZFN) sites to AAVS1 locus. Co-transfection with an AAVS1 targeted ZFN induces a double strand break and a non-homologous end joining repair mechanism,

resulting in mCherry-GAL9 insertion under an EF1 α promoter with a puromycin selection cassette. b Average copy number of puromycin genomic insertions per cell determined by droplet digital PCR, normalised to the reference gene AP3B1, as an indirect measurement of mCherry-GAL9 insertions. c Representative agarose gel of the amplicon spanning the AASV1 locus and the donor mCherry-GAL9 donor vector, confirming the insertion of the construct at the expected genomic location. Molecular weight (base-pairs, bp) of standards is indicated next to the gel. d Western blot of stably integrated mCherry-GAL9 cell lines for indicated proteins and non-transfected cell controls, 40 μ g per lane. e Fluorescence images of Huh7, HepG2, HeLa and NCI-H358 cells \pm insertion of the mCherry-GAL9 reporter under normal growth conditions, scale bar = 20 μ m. Note: LUTs between cell lines vary (\pm mCherry-GAL9 reporter are matched), this is intended for clarity of GAL9 signal within cells. See f for true fluorescent intensity. f Quantitation of cellular mCherry fluorescence intensity from reporter lines. Values are normalised means from n=3 independent experiments \pm SEM.

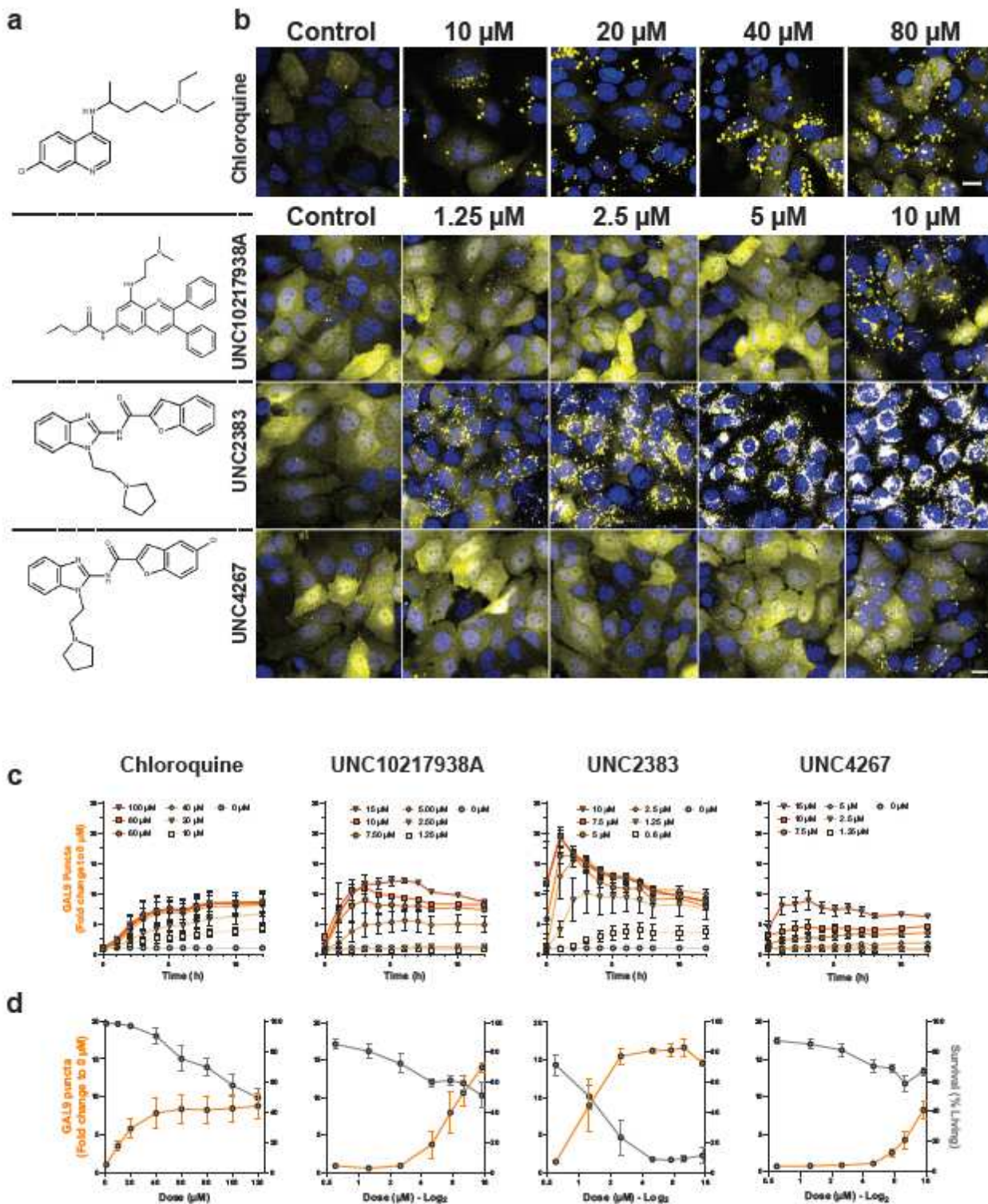


Figure 2

Small Molecules induce mCherry-GAL9 recruitment a Chemical structures of chloroquine and UNC compounds. b Representative images of Huh7 mCherry-GAL9 cells following 2 h incubation with indicated small molecules and dose, scale bar = 20 μm . c Kinetic analysis of mCherry-GAL9 puncta formed across 0-12 h of incubation with indicated compounds and doses, values represent normalised means \pm SEM from n=3 independent experiments. d Comparison of mCherry-GAL9 puncta induced (8 h

chloroquine, 2 h UNC compounds) to cell survival (12 h post-dosing, determined by Hoechst morphology) relative to the compound dose in Huh7 mCherry-GAL9 cells. Values represent normalised means \pm SEM from n=3 independent experiments.

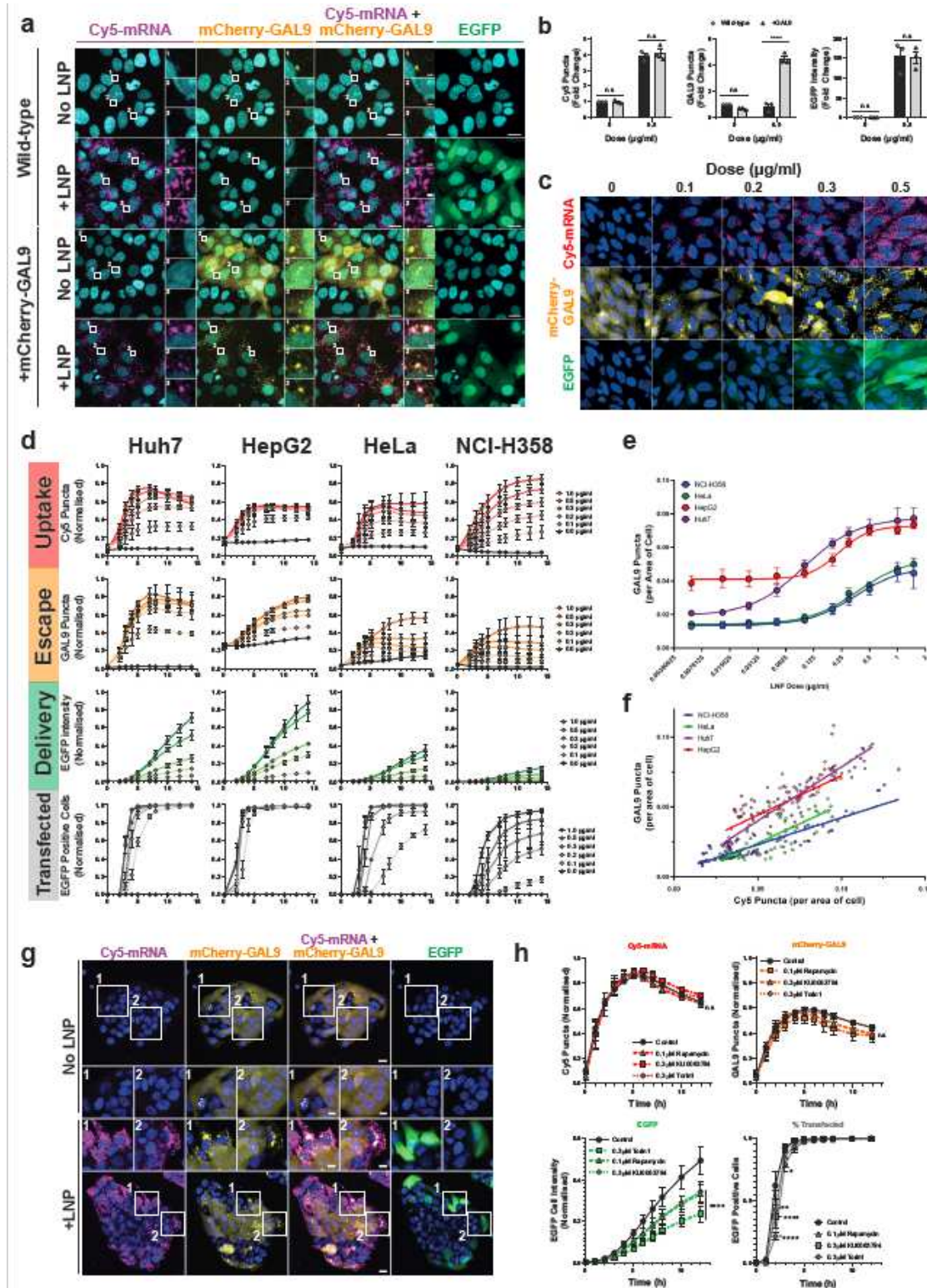


Figure 3

LNPs induce mCherry-GAL9 recruitment in Huh7 cells. Huh7 cells \pm mCherry-GAL9 reporter were dosed with 0.5 $\mu\text{g/ml}$ MC3-LNPs for 3 h and imaged live, scale bar = 20 μm , insets scale bar = 2 μm . **b** Quantitation of mCherry

GAL9 and Cy5-mRNA objects (3 h post-dosing) along with cellular EGFP intensity (12 h post-dosing) shown as fold-change to the untreated wild-type control from $n = 3$ independent experiments \pm SEM. c mCherry-GAL9 HeLa cells were treated with a dose range of MC3-LNPs (0-0.5 $\mu\text{g}/\text{ml}$) and imaged using live-cell microscopy at 10 h post-dosing, scale bar = 20 μm . d Quantitation of dose response in Huh7, HepG2, HeLa or NCI-H358 cells containing mCherry-GAL9 reporter across 0-14 h using 0-1 $\mu\text{g}/\text{ml}$ MC3-LNPs. Values indicate LNP uptake (Cy5-mRNA structures), endosomal escape (mCherry-GAL9 structures), mRNA delivery (EGFP fluorescence) and transfection (% EGFP positive cells). Values were normalised to 0-1 (min-max) per replicate and combined to represent normalised means from $n=3$ independent experiments. e Sum of GAL9 puncta per LNP dose across time course obtained in d was plotted against LNP dose per cell line. Four-parameter logistic curve with variable slope fitted for each cell line to mean values to obtain EC50 of LNP dose for GAL9 puncta induction. f Cy5 puncta were plotted against mCherry-GAL9 puncta across time course obtained in d per cell line, linear regression was fitted for each. Values obtained and fits for e,f are shown in supplementary table 1. g mCherry GAL9 NCI-H358 cells dosed with 0.5 $\mu\text{g}/\text{ml}$ MC3 and imaged after 10 h of incubation, scale bar = 20 μm , insets = 10 μm . h mCherry GAL9 Huh7 cells co dosed with 0.5 $\mu\text{g}/\text{ml}$ MC3 LNP and 0.3 μM Torin1, 0.3 μM KU0063794, 0.1 μM Rapamycin or DMSO control. Quantitation of indicated structures/cell intensity. Values represent normalised means from $n=3$ independent experiments \pm SEM. Significance was determined by two-way ANOVA followed by Dunnett's post-test to the DMSO control where * = $p < 0.05$, ** = $p < 0.01$, *** = $p < 0.001$, **** = $p < 0.0001$ and n.s= not significant.

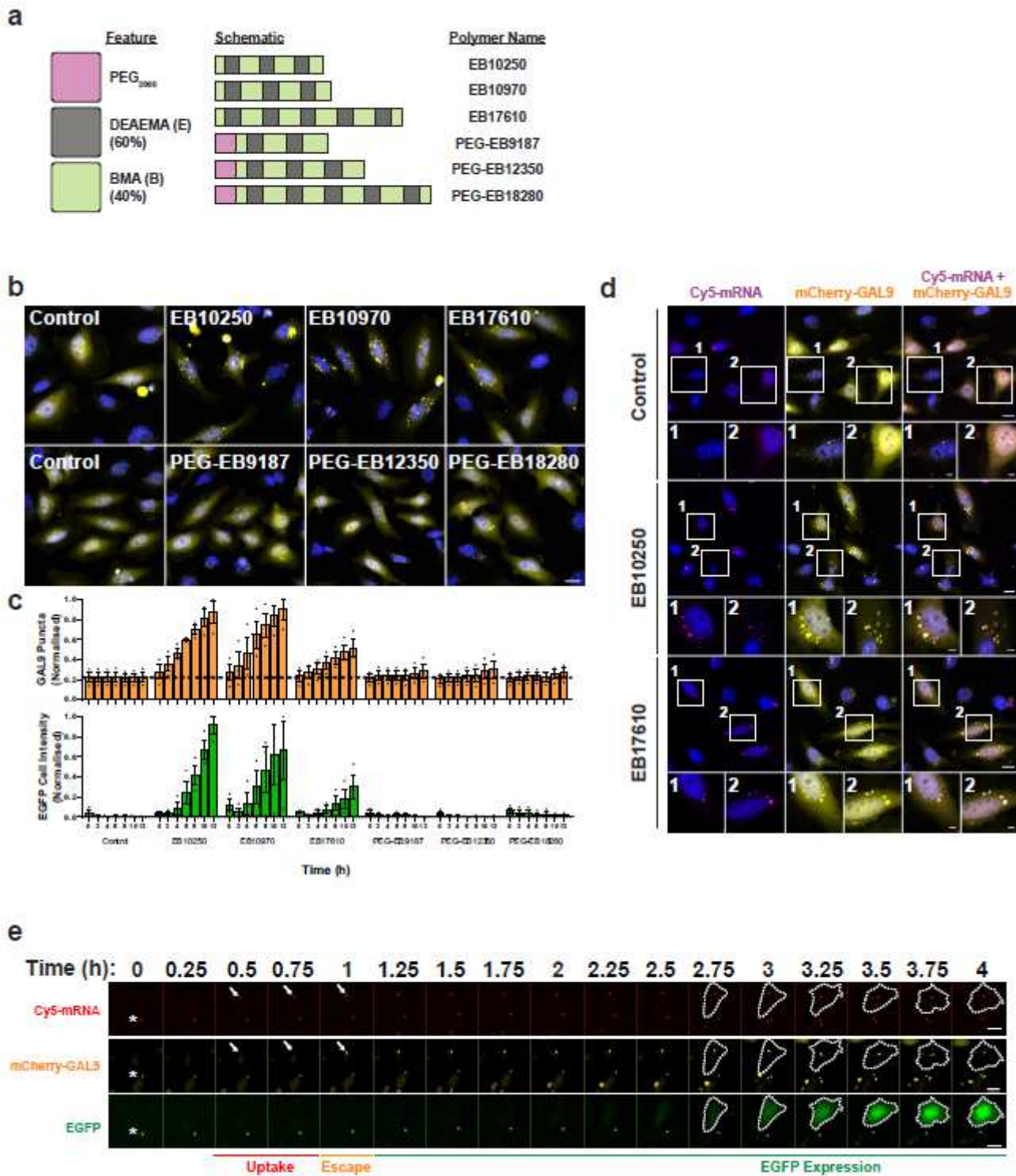


Figure 4

mCherry-GAL9 responds to polymeric nanoparticles a Overview of polymer names and compositions. Polymers are comprised of DEAEMA (60%) and BMA (40%) at variable lengths \pm PEG2000 first block. b Representative images of HeLa mCherry-GAL9 cells dosed with 1 μ g/ml of indicated polymers in serum free media and image by live cell microscopy, scale bar = 20 μ m. c Quantitation of mCherry-GAL9 structures and EGFP expression from b. d Representative images of HeLa mCherry-GAL9 cells treated

β -Sitosterol modifies endosomal escape rate a Huh7, HepG2, HeLa and NCI-H358 mCherry-GAL9 cells were dosed at indicated concentrations of MC3-LNPs formulated with cholesterol or β -sitosterol. Images are representative of 14 h post-dosing. Scale bar = 20 μ m. b Comparison of cell EGFP fluorescent intensity at 14 h after incubation with Cholesterol or β -sitosterol particles in Huh7, HeLa, HepG2 and NCI-H358 cells across 0.1-1.5 μ g/ml doses. Values represent normalised EGFP intensity \pm SEM from n=3 independent experiments. c Quantitation of a examining the formation of Cy5 positive structures, mCherry-GAL9 structures and EGFP fluorescence per cell over time. Values represent normalised means \pm SEM from n=3 independent experiments. Significance was determined in b,c for full 0-14 h time courses by two-way ANOVA followed by Tukey's multiple comparison test where * = $p < 0.05$, ** = $p < 0.01$ *** = $p < 0.001$, **** = $p < 0.0001$ and ns = not significant. d Comparison of total Cy5 or GAL9 puncta over time obtained from c for cholesterol or β -sitosterol particles in NCI-H358 cells. Linear regression carried out and R² values displayed on the graph.

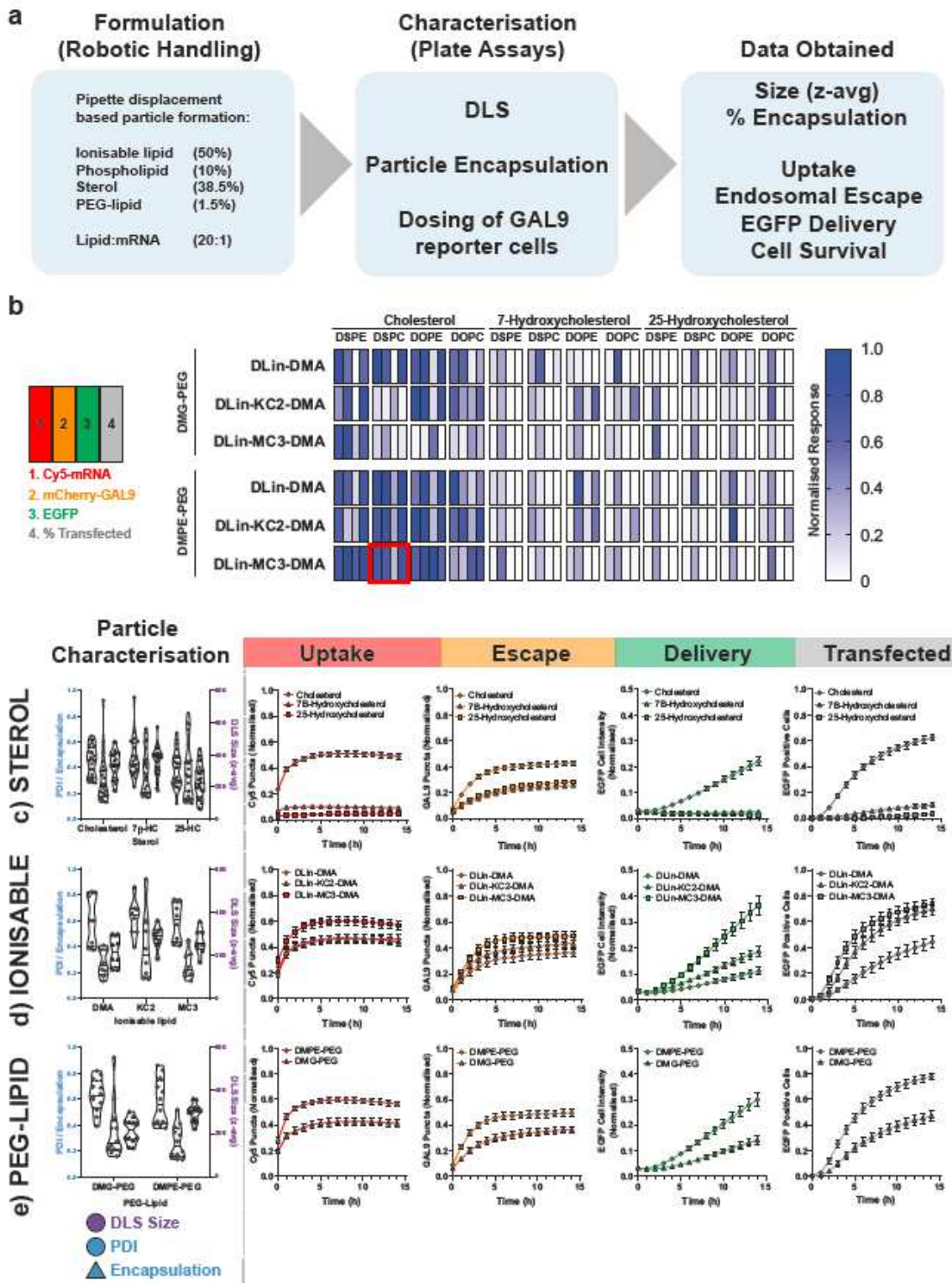


Figure 6

Use of mCherry-GAL9 reporter line with automated particle formulation a Overview of experimental approach, particles are formed by automated pipetting in a plate-based format and feed directly into plate-based assays for particle size by dynamic light scattering (DLS), encapsulation by ribogreen integration and for dosing mCherry-GAL9 reporter cells directly. b Heatmap summary of LNP formulation variation data representing normalised Cy5-mRNA uptake, mCherry-GAL9 puncta, EGFP fluorescence and

% EGFP positive cell values at 14 h post-dosing. Red square indicates standard composition of particles commonly used in rest of manuscript. c,d,e Overview of particle characteristics and kinetic results obtained with the screening approach looking at comparisons of particles based upon variable components. Particle plots indicate individual particle size (diameter, nm), PDI and mRNA encapsulation (where 0.2 = 20%). Solid line = median value, dashed line = quartiles. Cellular values plotted are mean normalised values \pm SEM c Sterol modified particles, n = 24 LNPs per group from n = 4 experiments. d Ionisable lipid modified, only data with cholesterol particles shown, n= 8 per group from n = 4 experiments e PEG-lipid modified, only data with cholesterol particles shown, n= 12 per group from n= 4 experiments.

Supplementary Files

This is a list of supplementary files associated with this preprint. Click to download.

- [SupplementaryFiguresLegends.pdf](#)
- [SourceDataFile.xlsx](#)